International Journal of Heat and Mass Transfer 137 (2019) 42–51

Contents lists available at ScienceDirect

International Journal of Heat and Mass Transfer

journal homepage: www.elsevier.com/locate/ijhmt

Thermal modeling and comparative analysis of jet impingement liquid cooling for high power electronics

Ruikang Wu, Tao Hong, Qingyu Cheng, Hao Zou, Yiwen Fan, Xiaobing Luo *

State Key Laboratory of Coal Combustion, School of Energy and Power Engineering, Huazhong University of Science and Technology, Wuhan 430074, China

ARTICLE INFO

Article history:
Received 25 January 2019
Received in revised form 14 March 2019
Accepted 19 March 2019

Keywords:
Thermal model
Jet impingement
Direct liquid cooling
High power electronics
Thermal resistance

ABSTRACT

Thermal management of high-power electronic devices has become the bottleneck that restricts the working performance. Taking fully advantage of the cooling potential is urgently required. However, most existing direct liquid cooling methods only consider the cooling of the top surface of the electronic devices/chips, causing insufficient utilization of exposed chip surfaces. In this paper, a jet impingement body cooling device (JIBC) and a channel/jet impingement hybrid body cooling (HBC) device with micro-nozzles using the traditional mechanical machining method were developed. The body cooling devices provide high efficient cooling to the top surface and the side surfaces of the chip. The cooling performance were tested by experiments and it is found to be better than the traditional direct liquid cooling method. The total thermal resistance of 0.041 k/W, which can be compared to the thermal resistance of the thermal interface material, was achieved by the JIBC device when the flow rate is 1800 mL/min. The thermal model for the developed cooling methods was established to predict the chip temperature and characterize the heat transfer mechanism. It is found that the critical nozzle diameter exists, which determines which one of the two developed body cooling device has the better cooling performance. The proposed thermal model is found to be necessary for the quick design and optimal design of the body cooling device for high power and high heat flux electronics.

1. Introduction

Due to the increasing integration density, thermal management of high power electronics, such as the insulated gate bipolar transistors (IGBTs), the high electron mobility transistors (HEMTs), the light emitting diodes (LEDs) and the high-performance computing chips, has become one of the major challenges [1–9]. With the growing need for performance, several hundred watts of heat may be generated in the electronics with a millimeter size. Liquid cooling is the mainstream method to control the temperature of high power electronics within a proper range, owing to its large heat transfer efficiency and the compactness [10,11]. Most liquid cooling heat sinks are attached to the electronic device by the thermal interface material (TIM) to reduce the contact thermal resistance, which is called the indirect liquid cooling [12–14]. However, the large thermal resistance caused by the low thermal conductivity of the TIM is the major obstacle for thermal management of high power electronics. Although massive researches have been done to increase the thermal conductivity of the TIM [15,16], it is still far from meeting the requirements of engineering applications. Therefore, the direct liquid cooling, which eliminates the contact thermal resistance by making the coolant directly touch the electronics, is a better option for heat dissipation of electronics with high heat flux.

Jet impingement and spray cooling are both commonly used direct liquid cooling techniques [17,18]. Spray cooling was reported to have the highest heat dissipation capability owing to the boiling of the micron liquid droplets [19,20]. However, the system complexity, critical heat flux and the instability caused by vapor and bobbles limit its application. Jet impingement liquid cooling with array has also been studied by many researchers in the past decades [21–23]. The heat transfer and flow mechanism of the free, submerged and confined imping liquid jets have been fully investigated by theory, numerical simulation and experiments [24–28]. When the jet flow is ejected to a surface, very thin hydrodynamic and thermal boundary layers form in the impingement region, resulting in extremely high heat transfer coefficients within the stagnation zone. Garimella et al. experimentally investigated the influence of fluid thermos-physical properties on the heat transfer from confined and submerged impinging jets [27], and the generalized correlations for stagnation-point Nusselt number and area-averaged Nusselt-number were obtained. Confined jet impingement direct liquid cooling is often used to cool the

* Corresponding author.
E-mail address: luoxb@hust.edu.cn (X. Luo).

https://doi.org/10.1016/j.ijheatmasstransfer.2019.03.112
0017-9310/

electronics because of its compact structure. Bandhauer et al. developed a jet impingement direct liquid cooling device with for high performance ICs, and the average heat transfer coefficient of 13,100 $W\,m^{-2}\,K^{-1}$ was achieved using a nozzle diameter of 300 μm [29]. However, the heat sink device was made of epoxy by using the 3D printing method, which is unreliable in high temperature and the lifetime is short. Jorg et al. presented an approach of direct single jet impingement liquid cooling of a typical metal-oxidesemiconductor field-effect transistor (MOSFET) power module [30]. Heat transfer coefficient up to 12,000 $W\,m^{-2}\,K^{-1}$ was achieved using only 10.8 cm^2 assembly space for the cooling device. Besides, the hybrid micro-channel jet impingement cooling method was proposed and studied to enhance the heat transfer of jet impingement cooling [31–34].

However, almost all the previous studies about the jet impingement direct liquid cooling were focused on cooling the top surface of the electronic device or the chip. The existence of the thickness of the chip may cause large temperature rise inside the chip under a large heat load. The thickness of the electronic components or chips could be as large as several millimeters, especially for the high power electronic packaging unit [35]. In addition, there are various shapes and sizes of the electronics, which might cause the ratio of the top surface area to the overall surface area very small. In such cases, traditional direct liquid cooling on the top surface would not be sufficient for temperature control of the high power electronics with a certain thickness. Therefore, direct liquid cooling on all the available surfaces of the electronic component is required to decrease its temperature rise, taking fully advantage of the heat dissipation area. This cooling method is called body cooling in this work, which is also known as the side and end cooling [36,37]. However, there are few studies about the body cooling jet impingement. In addition, the thermal model of the direct liquid body cooling method has not been developed, which is not convenient for the structure design and optimization of the body cooling methods.

In this work, we developed a jet impingement body cooling (JIBC) device and a channel/jet impingement hybrid body cooling (HBC) device using the traditional mechanical machining method with micro-nozzles. The thermal model for the JIBC, HBC and traditional jet impingement surface cooling (JISC) was established. The thermal model is helpful to guide the structure design of the JIBC, HBC and JISC. The heat dissipation capability of the three cooling method were compared by theory, numerical simulation and experiments.

2. Thermal model

The developed JIBC and HBC structures are shown in Fig. 1(a) and (b). The traditional jet impingement surface cooling structure is shown in Fig. 1(c). In the JIBC case, the jet impingement nozzles are set opposite to all the surfaces of the heated chip to let the coolant directly impinge to the exposed surfaces of the heated chip. In the HBC case, however, the nozzles are only set opposite to the top surface of the heated chip, so that the coolant can only be ejected to the top surface. After being ejected to the top surface, the coolant flows through the side surfaces of the heated chip to cool these surfaces, and then flows out of the device. Thus, the HBC combines jet impingement cooling for the top surface of the chip and channel cooling for the side surfaces. If some micro structures are machined at the side surfaces of the chip or the corresponding opposite walls, the channel cooling may turn to the mini/microchannel cooling. To make it simple, the microchannel configuration was not investigated in this work. In the JISC case, the nozzles are also set opposite to the top surface of the heated chip. After being ejected to the top surface, the coolant directly flows out of the device without touching the side surfaces.

2.1. Surface heat transfer coefficient

During the engineering design, the edge length of the chip probably may not be divided evenly by the designed jet-to-jet spacing *S*. *S* is the square unit cell dimension of the jet impingement array footprint [38]. For this reason, as is shown in Fig. 2(a), some part of the array footprint may be missing on the chip surface, and some extra part may exist. Therefore, the area-averaged convective heat transfer coefficient cannot be simply calculated by using correlations for the area-averaged Nusselt number in literatures. The chip surface must be discretized to obtain the local convective heat transfer coefficient $h(x, y)$. We only consider single-phase liquid cooling in this work. The single-phase heat transfer profile of the jet impingement is verified as a bell-shaped local heat transfer coefficient distribution with a maximum value at the stagnation point and a monotonic decrease in the outward radial direction [24]. The local convective heat transfer coefficient can be obtained by

$$h'(r) = \left[C_1 - C_2 \exp\left(\frac{-r^2}{2}\right)\right]^{-1} \tag{1}$$

where C_1 and C_2 can be calculated by the stagnation Nusselt number and the area-averaged Nusselt number of the array footprint.

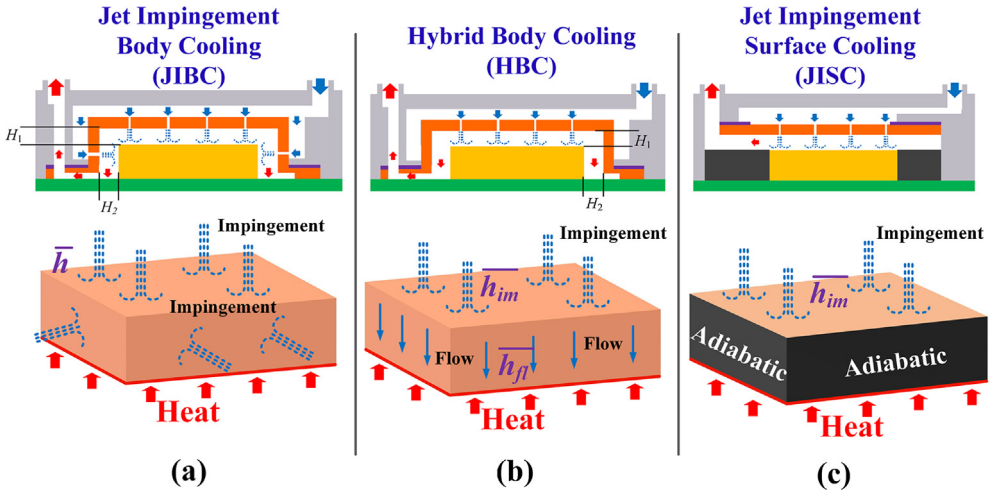

Fig. 1. Schematic diagram of (a) the jet impingement body cooling, (b) the hybrid body cooling and (c) the traditional jet impingement surface cooling.

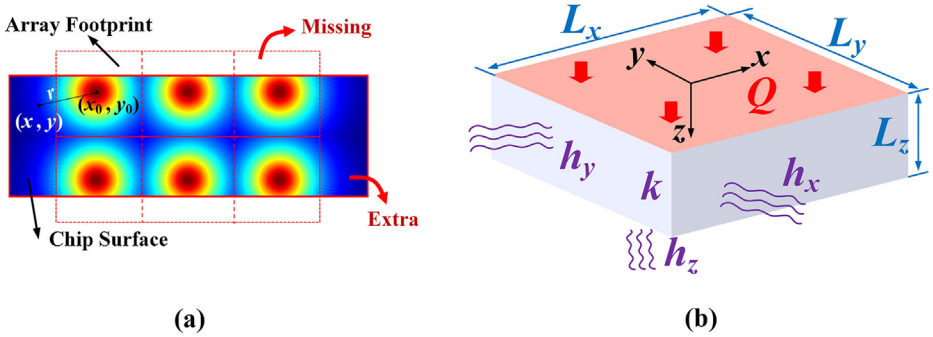

Fig. 2. The schematic diagram of (a) the distribution of the convective heat transfer coefficient on the surfaces and (b) the chip with body cooling.

These two numbers were calculated by using the empirical correlations that was verified by experiments previously. The stagnation Nusselt number is given by [27]

$$Nu_0 = 1.409Re^{0.497}Pr^{0.444}(l/D)^{-0.058}(2r_{eq}/D)^{-0.272} \tag{2}$$

where $r_{eq} = S/\sqrt{\pi}$ and l is the nozzle length. D is the nozzle diameter. The area-averaged Nusselt number of the array footprint is given by [39]

$$\overline{Nu} = 0.5Re^{.667}Pr^{0.42}(l/D)^{-0.058}\left[1+\left(\frac{(H/D\sqrt{\pi}/2)}{0.6(S/D)}\right)^6\right]^{-0.05} \times\left(\frac{\sqrt{\pi}}{S/D}\right)^{\frac{1-1.1\sqrt{\pi}/(S/D)}{1+0.1(H/D-6)\sqrt{\pi}/(S/D)}} \tag{3}$$

where H is the jet-to-target spacing, which is shown Fig. 1 as H_1 and H_2. The calculation of C_1, C_2 and more details about calculating the $h'(r)$ may be found in Ref. [37]. Thus, the local convective heat transfer coefficient $h(x, y)$ can be calculated by

$$h(x,y) = h'\left(\sqrt{(x-x_o)^2+(y-y_o)^2}\right) \tag{4}$$

where (x_0,y_0) is the coordinate of the nozzle closest to the point (x, y). And the area-averaged surface convective heat transfer coefficient of the chip surface is calculated as

$$\bar{h} = \left[\frac{1}{A}\iint\frac{1}{h(x,y)}dxdy\right]^{-1} \tag{5}$$

where A is the surface area. The jet impingement heat transfer coefficient $\overline{h_{im}}$ of the HBC and JISC can be calculated by the method mentioned above, with Re calculated by using V'_D.

We assumed that the channel flow of the coolant through the side surfaces of the chip is uniform. Thus, the downward flow velocity can be calculated by

$$V_{side} = \frac{Q_v}{2(L_x+L_y)H_2} \tag{6}$$

where Q_v is the total volume flow rate of the coolant, L_x and L_y are edge lengths of the top surface of the chip. The channel flow is usually laminar flow because of the small equivalent diameter. In this work, the laminar channel flow is regarded as the fluid flowing through the plate. Therefore, the heat transfer coefficient of the side surfaces in the HBC is given by

$$\overline{h_{fl}} = 0.664\frac{k_f}{L_z}Re_{fl}^{0.5}Pr^{1/3} \tag{7}$$

where k_f is the thermal conductivity of the coolant, L_z is the thickness of the chip and $Re_{fl} = \rho V_{side}L_z/\mu$. ρ and μ are the density and viscosity of the coolant, respectively.

2.2. Body cooling thermal conductive model

As is shown in Fig. 2(b), when the uniform heat flux Q is added to one surface of the chip, if the area-averaged convective heat transfer coefficients of the side and end walls of the chip are known, the temperature field $T(x, y, z)$ of the chip can be obtained. The temperature field $T(x, y, z)$ should be obtained according to the steady state thermal conduction equation in three dimensions, given as:

$$\nabla^2 T = \frac{\partial^2 T}{\partial x^2}+\frac{\partial^2 T}{\partial y^2}+\frac{\partial^2 T}{\partial z^2} = 0 \tag{8}$$

The boundary conditions are prescribed as follows:

$$\begin{aligned}
&x = \tfrac{L_x}{2},\ \tfrac{\partial T}{\partial x} = 0\\
&x = 0\ or\ L_x,\ \tfrac{\partial T}{\partial x}+\tfrac{h_y}{k}(T-T_f) = 0\\
&y = \tfrac{L_y}{2},\ \tfrac{\partial T}{\partial y} = 0\\
&y = 0\ or\ L_y,\ \tfrac{\partial T}{\partial y}+\tfrac{h_x}{k}(T-T_f) = 0\\
&z = 0,\ \tfrac{\partial T}{\partial z}+\tfrac{Q}{L_xL_yk} = 0\\
&z = L_z,\ \tfrac{\partial T}{\partial z}+\tfrac{h_z}{k}(T-T_f) = 0
\end{aligned} \tag{9}$$

where k is the thermal conductivity of the chip, h_z is the area-averaged heat transfer coefficient of the top surface of the chip ($\bar{h}$ and $\overline{h_{im}}$), h_x and h_y are the corresponding area-averaged heat transfer coefficient of the side surfaces. According to the method of separation of variables, the temperature field is given as

$$T(x,y,z)-T_f = \sum_{m=1}^{\infty}\sum_{n=1}^{\infty}\cos(\lambda_{xm}x)\cos(\lambda_{ym}y) \times[A_{mn}\cosh(\beta_{mn}z)+B_{mn}\sinh(\beta_{mn}z)] \tag{10}$$

where T_f is the fluid temperature, which is assumed to be the inlet fluid temperature of the heat sink, λ_{xm}, λ_{yn} and β_{mn} are the eigenvalues and are obtained from iterative solution of the following equations:

$$\lambda_{xm}\sin\left(\frac{\lambda_{xm}L_x}{2}\right) = \frac{h_y}{k}\cos\left(\frac{\lambda_{xm}L_x}{2}\right) \tag{11}$$

$$\lambda_{yn}\sin\left(\frac{\lambda_{yn}L_y}{2}\right) = \frac{h_x}{k}\cos\left(\frac{\lambda_{yn}L_y}{2}\right) \tag{12}$$

$$\beta_{mn} = \sqrt{\lambda_{xm}^2+\lambda_{yn}^2} \tag{13}$$

and A_{mn} and B_{mn} are obtained from the following equations:

$$A_{mn} = -B_{mn}\frac{k\beta_{mn}+h_z\tanh(\beta_{mn}L_z)}{h_z+k\beta_{mn}\tanh(\beta_{mn}L_z)} \tag{14}$$

$$B_{mn} = \frac{-4Q\sin(\lambda_{xm}L_x/2)\sin(\lambda_{yn}L_y/2)}{kL_xL_y\beta_{mn}[\sin(\lambda_{xm}L_x)/2+\lambda_{xm}L_x/2][\sin(\lambda_{yn}L_y)/2+\lambda_{yn}L_y/2]} \tag{15}$$

More details about calculating the temperature field may refer to Ref. [40].

3. Experiment

The heat sink device of the three cooling cases were designed, manufactured and tested by experiments. The structure of the JIBC device is shown in Fig. 3(a). Rather than using the 3D printing method to manufacture the whole device with epoxy in one-piece, the device is separated to be composed of three components: the shell, the gasket and the nozzle substrate, which were all machined by traditional mechanical CNC machining method with aluminum alloy. As shown in Fig. 3(b), nozzles with diameter of 300 μm were machined by electro-sparking method on the side-walls of the nozzle substrate. The viton rubber gasket was set between the gap of the nozzle substrate and the shell to prevent the leakage and make sure that all the coolant flows through the nozzles. The gasket and nozzle substrate were fixed to the shell by screws. In the JIBC case, nozzles were machined on the top wall and side walls (left, front, right and back walls). However, in the HBC case, the jet impingement nozzles were not machined on the side walls, but only machined on the top wall of the nozzle substrate. As is shown in Fig. 1(c), the nozzle substrate of the JISC case was machined as a plate with jet impingement nozzles for the top surface of the chip, which is similar to the traditional structures in previous studies. The device has a long life and is reliable even in the high temperature environment.

The nozzle arrangement for the JIBC case is shown in Fig. 3(c). The nozzle arrangements of the top wall in the HBC case and the JISC case are the same as in the JIBC case. More details about the nozzle arrangement of the three cases are listed in Table 1, in which N is the nozzle number. The size of the heated chip is 10 mm × 50 mm × 4 mm and the chip was made of copper.

The test facility in this work is schematically shown in Fig. 4. DI-water is circulated through the flow loop driven by a hydrodynamically levitated centrifugal micropump [41–43]. The flow rate can be set by tuning the rotation speed of the micropump and by the valve. The volume flow rate is measured by a turbine flow meter (YF-S401) with ±2% accuracy. The air-cooled heat exchanger with 16 copper pipes was used to cool the coolant and remove the heat to the ambient. A 40 μm filter was positioned upstream of the heat sink to prevent blocking caused by impurities in the coolant. A water tank was assembled upstream of the filter and a thermocouple was put inside the water tank to measure the inlet coolant temperature. The inlet fluid temperature was controlled at 40 °C stably by tuning the rotating speed of the fans in the air-cooled heat exchanger in all the experiments. Seven heating rods were inserted in the copper block to provide the heating power. In order to prevent the heat loss, the thermal insulation cotton was used to wrap the copper block up. The maximum heating loss was briefly calculated using the Newton's law of cooling $q_{loss} = h_n \times A_c \times (T_c - T_a)$ with the maximum heating power (800 W), where h_n is the natural convective heat transfer coefficient, A_c is the surface area of the copper block, T_c is the cotton temperature and T_a is the ambient temperature. In maximum, we set h_n to be 10 W/m^2 K. By measuring the cotton and ambient temperature, the heat loss was calculated to be 15.97 W with heating power of 800 W, meaning that the heat loss was no more than 2%.

Table 1
Structure parameters of the nozzle substrate.

		JIBC	HBC	JISC
	D [μm]	300	300	300
	S [μm]	4550	4550	4550
Top	N	2 × 11	2 × 11	2 × 11
	H [μm]	400	400	400
Left	N	2 × 1	\	\
	H_2 [μm]	400	400	\
Front	N	1 × 11	\	\
	H_2 [μm]	400	400	\

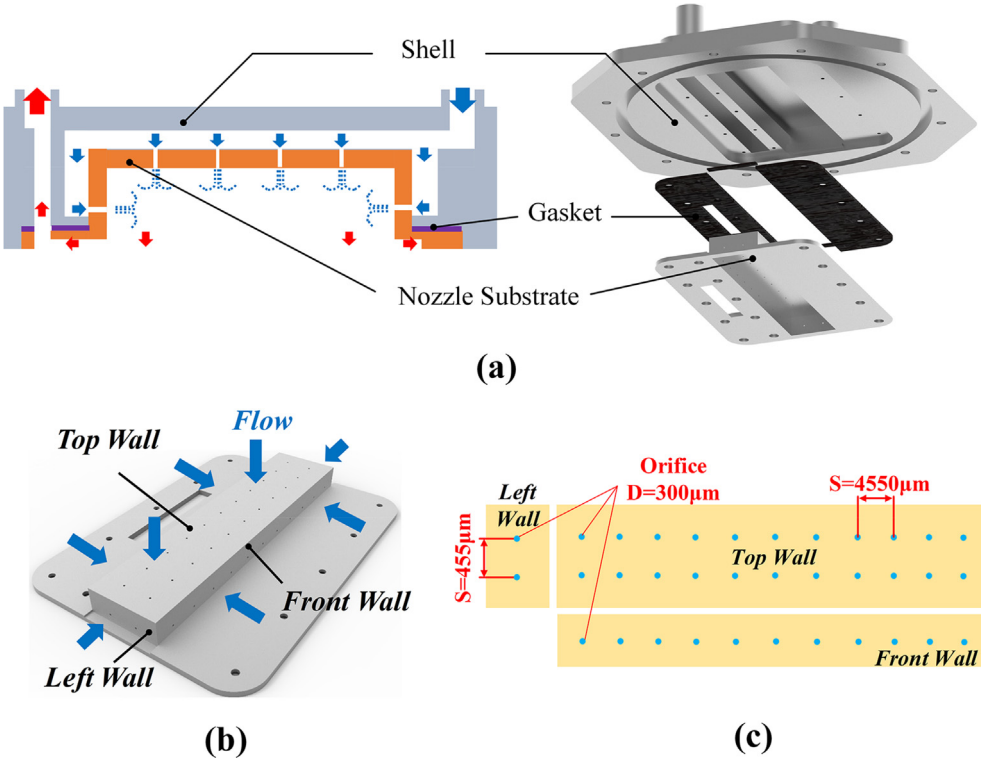

Fig. 3. The schematic diagram of (a) the structure of the JIBC device, (b) the structure of the nozzle substrate and (c) the nozzle arrangement on the nozzle substrate walls.

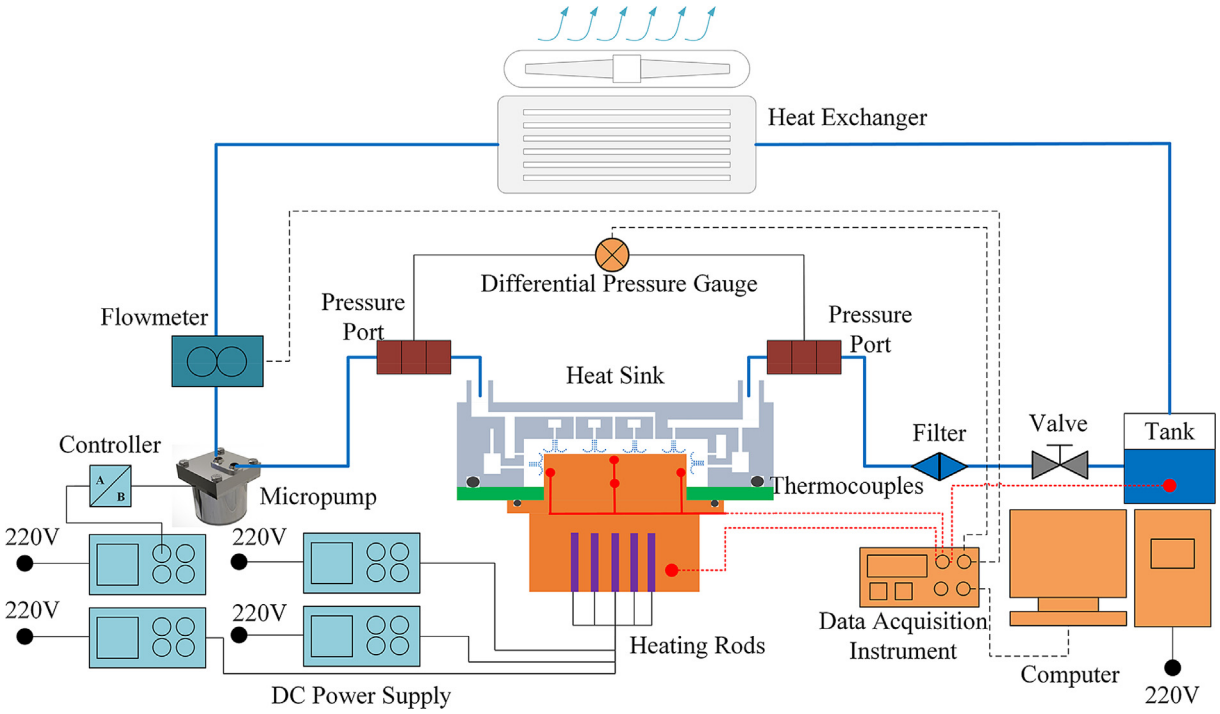

Fig. 4. The system diagram of the test facility.

4. Numerical simulation

Numerical simulations were done to investigate the heat transfer and fluid flow mechanism by using the commercial multiphysics software COMSOL MULTIPHYSICS 5.3a. The Heat Transfer and CFD packages were coupled in this study. To reduce the computational costs, only the dominant fluid domain was considered in the simulation, as is shown in Fig. 5, rather than using the whole fluid domain of the heat sink device. To characterize the heat transfer and fluid flow process more accurately, grids were meshed finer in the jet impingement zone. The nozzle orifices were set as the fluid inlet. The inlet fluid temperature was set to be 40 °C. Boundary heat source was added on the bottom surface of the chip. The material of the chip was set as copper and the coolant was the DI-water. The physical property parameters of the materials used in the numerical simulation are listed in Table 2. The grid independence test was done. The maximum temperature of the chip of the JIBC case was calculated with the grids number of 313135, 702516, 1922799 and 2289566. The discrepancies were less than 5.5%. Taking the computational cost into consideration, the mesh parameters with grid number of 702516 were used in all the simulations, meaning that the 'Normal' grid was selected in the COMSOL.

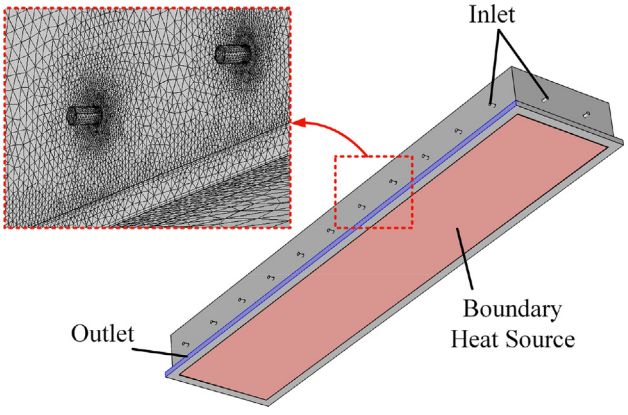

Fig. 5. Simulation model of the JIBC.

Table 2
The physical property parameters of materials used in the numerical simulation.

Material	k (W/m·K)	ρ (kg/m3)	μ (mPa·s)	c_p (J/Kg·K)	$T_{fluid,in}$ (°C)
Water	0.635	992.2	0.6533	4174	40
Pure Copper	380	/	/	/	/

5. Results and discussion

As the chip is cooled by all the exposed surfaces, the temperature field inside the chip is high non-uniform. Therefore, the average temperature of the chip is not easy to be characterized. Thus, the maximum temperature of the chip was used to analyze the cooling performance in this work. In the experiment, we put seven separated thermocouples at the bottom surface region of the chip to measure the maximum temperature. As the inlet fluid temperature was controlled to be 40 °C in the model, simulation and the experiment, the maximum temperature rise $\Delta T_{max} = T_{max} - T_f$ was used in the following results, where T_{max} is the maximum temperature. Experimental results of the maximum temperature rise versus the heating power of the JIBC, HBC and JISC cases are shown in Fig. 6. It can be seen that the maximum temperature rise changes linearly with the heating power, indicating that the total thermal resistance is independent on the heat load, which is the general result that obtained using the single-phase liquid cooling. When the volume flow rate increases from 1000 mL/min to 1500 mL/min, the maximum temperature decreases, and the difference becomes larger with increasing the heat load. According to the results shown in Fig. 6(a), the temperature difference between the experimental and model of the JIBC case is less than 8.0%. Similarly, results in Fig. 6(b) and (c) indicate that the

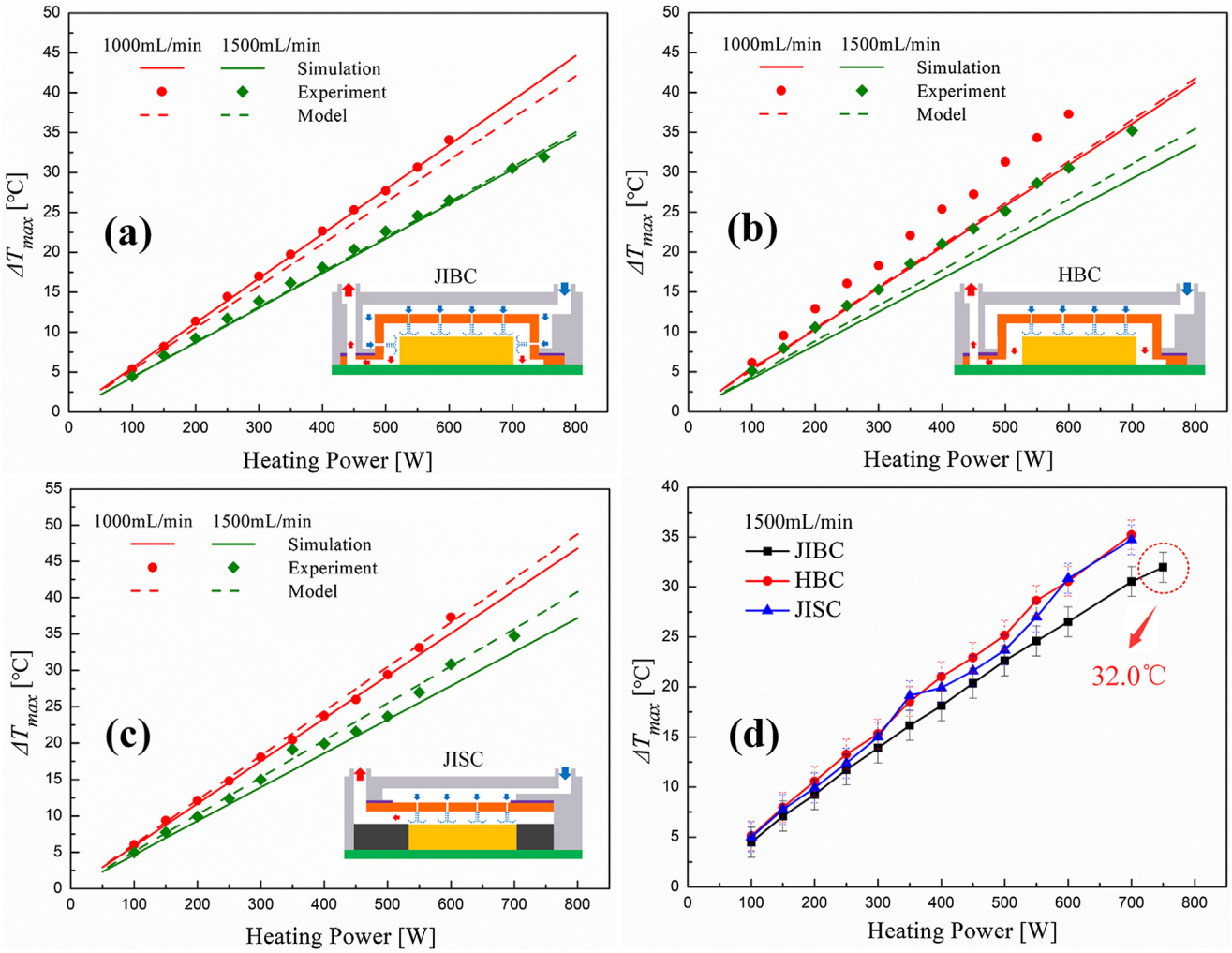

Fig. 6. The maximum temperature rise versus the heating power (a) of the JIBC case, (b) of the HBC case, (c) of the JISC case and (d) of the three different cooling cases obtained by experiments with the volume flow rate of 1500 mL/min.

temperature differences between the experiment and model of the HBC and JISC cases are less than 18.1% and 6.2%, respectively. Thus, results of the experiment, simulation and model are in a good agreement. The measured maximum temperature of the HBC is slightly higher than that obtained by simulation and model. Because the flow velocity of the side-wall channel cooling is mainly dominated by the channel width H_2, where the machining and assembly errors may exist. From the experimental results shown in Fig. 6(d), it can be observed that the JIBC has the best cooling performance. When the heating power is as large as 750 W, the maximum temperature rise of the chip is only 32.0 °C with the flow rate of 1500 mL/min by using the JIBC.

The range of the jet Reynolds number is from 1344 to 4030 in this work. The jet flow is transition flow with Reynolds number from 1344 to 3000, and turbulent flow with Reynolds number from 3000 to 4030. Therefore, the jet flow was assumed to be turbulent in the COMSOL simulation. Experimental results of the maximum temperature rise versus the volume flow rate of the JIBC, HBC and JISC cases with the heat power of 500 W are shown in Fig. 7. The maximum temperature rise decreases with increasing the volume flow rate. The trend of results indicate that the temperature would not decrease much when the flow rate is very large, because the convective heat transfer coefficient would be large enough so that the thermal conductive resistance of the chip dominates.

According to results shown in Fig. 7(a), the temperature difference between the experimental and model of the JIBC case is less than 10.8%. Results in Fig. 7(b) and (c) indicate that the temperature differences between the experiment and model of the HBC and JISC cases are less than 21.0% and 19.3%, respectively. The difference between experiment and model is main due to the assumptions and the accuracy of the adopted empirical heat transfer correlations. Even so, the model still fits well with the simulation. Within the margin of errors, the developed thermal model is accurate enough for the heat transfer study, quick design and structure optimization of the JIBC, HBC and JISC. Fig. 7(d) shows the experimental results of the maximum total thermal resistance, which is given as $R_{total} = (T_{max} - T_f)/Q$. The decreasing trends of the three devices are the same. We experimentally obtained the minimum total thermal resistance of 0.041 k/W by using the JIBC with the volume flow rate of 1800 mL/min. As a comparison, the thermal resistance of the commercial TIM with high thermal conductivity of 3 $W\,m^{-1}\,K^{-1}$ is as large as 0.033 k/W, considering the thickness of 50 μm and the surface size of 10 mm × 50 mm. Therefore, the extremely low total thermal resistance was obtained.

In Fig. 8(b) we can see that the heat dissipation capability for the top surface of the HBC and JISC are almost the same. However, the HBC can provide extra cooling for the chip by channel cooling to the side surfaces, which is not available by the JISC. That's the

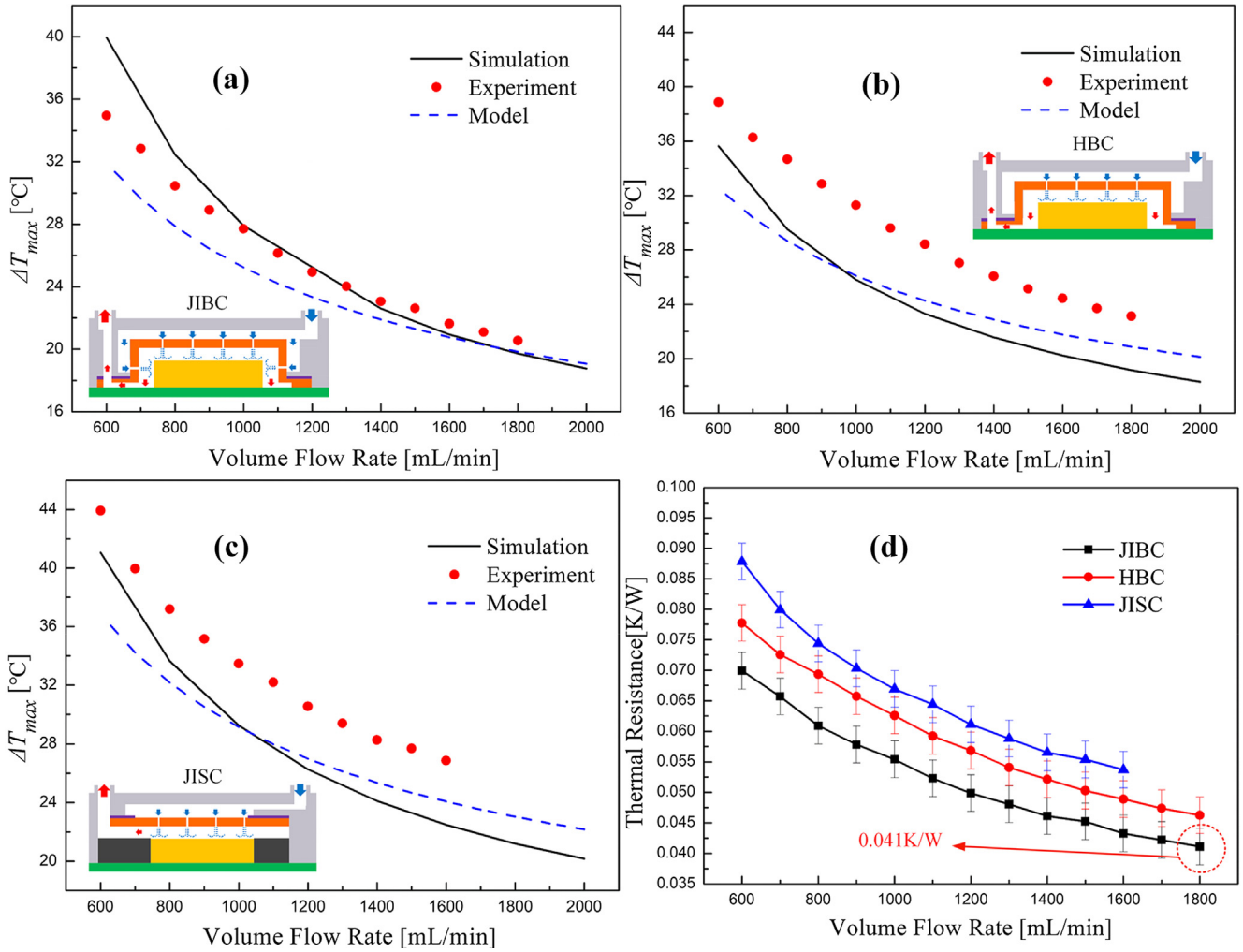

Fig. 7. The maximum temperature rise versus the volume flow rate (a) of the JIBC case, (b) of the HBC case, (c) of the JISC case, and (d) maximum thermal resistance versus the volume flow rate of the three different cooling cases obtained by experiments with the heating power of 500 W.

reason why the HBC has lower total thermal resistance than the JISC shown in Fig. 7(d), although the side cooling h is only nearly 1/4 of the top cooling h of the HBC. Fig. 8(a) shows the simulated and modeled jet impinging heat transfer coefficient of the top, left and front surfaces in the JIBC case. The model calculated h fits well with the simulated results. Although the nozzle parameters of all the nozzle substrate walls are set as the same, the jet impinging heat transfer coefficient for the top, left and front surfaces are all different. This is mainly due to the missing and extension of the array footprint as described in Section 2.2 and Fig. 2(a).

Owing to the chip size and the nozzle arrangement, the JIBC provides the maximum heat transfer coefficient for the front and back surface, and the minimum heat transfer coefficient for the top surface. In the JIBC case, the diameters of all the nozzles were set to be same, so that the flow rate at each nozzle was assumed to be equal. The fluid flow velocity at the nozzles can be calculated as

$$V_D = \frac{Q_v}{(N_{top} + 2N_{front} + 2N_{right})A_D} \tag{16}$$

where N_{top}, N_{front} and N_{right} are the nozzle number at the top, front and right surface, respectively. $A_D = \pi D^2/4$ is the nozzle area. The flow velocity at the nozzles for the HBC and JISC is given by

$$V'_D = \frac{Q_v}{N_{top}A_D} \tag{17}$$

The nozzle Reynolds number Re can be calculated according to the nozzle flow velocity. In this work, the nozzle number of the JIBC is 48, and that of the HBC and JISC are both 22. Therefore, the nozzle flow velocity of the HBC and JISC is more than 2 times as that of the JIBC, leading to much larger heat transfer coefficient for the top surface. Although the top surface heat transfer coefficient of the HBC and JISC is more than 2 times as the JIBC, the total thermal resistance of the JIBC is still lower than all the other cooling devices (Fig. 7(d)). The reason is that the heat transfer coefficients for the side surfaces of the JIBC are nearly 2 times larger than that of the HBC, which confirmed that the side cooling is quite important.

The heat flux ratio of the surface is calculate by $\eta = Q_{sur}/Q$, where Q_{sur} represent the heat that dissipated from the surface. Obviously, the heat flux ratio of the top surface in the JISC case is 100%. As is shown in Fig. 9, nearly 75% of the heat is dissipated from the top surface in the HBC case, while only less than 45% of the heat is dissipated from the top surface in the JIBC case. Much more heat is dissipated from the side surfaces of the JIBC because of the larger h of the side surfaces. Although the sum of the area of the front and back surfaces is only 80% of the area of the top surface, the dissipated heat from the front and back surfaces is larger than that from the top surface in the JIBC, which is mainly owing to the larger side cooling h than the top surface.

Fig. 10 shows the simulated surface temperature field of the JIBC, HBC and JISC. The temperature field clearly reflects the

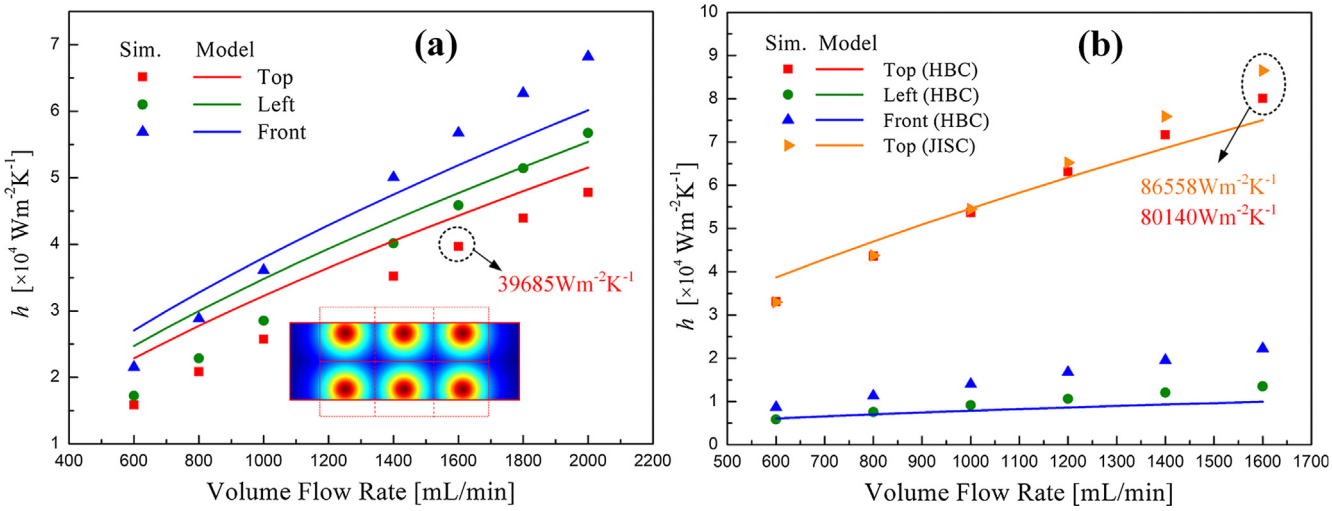

Fig. 8. The convective heat transfer coefficient of the chip surfaces for (a) the JIBC and (b) the HBC and the JISC.

arrangement of the jet impingement nozzles. We can see that the temperature at the edges and corners of the chip is much lower in the JIBC and HBC case due to the body cooing effect. The same result does not exist in the JISC case without body cooling. The nozzle flow velocity of the JIBC is only 4.91 m/s, while that of the HBC and JISC cases are both 10.72 m/s. The larger nozzle flow velocity results in greater heat dissipation capability, leading to the lower top surface temperature of the HBC than the JIBC. Although the top surface heat dissipation capability of the HBC and the JISC are equal, the top surface temperature of the JISC is much higher, because of the larger heat flux. Different from the other two cases, the temperature field of the HBC shows obvious asymmetry. This result indicates that flow in the HBC is more sensitive to the pressure difference between the inlet and the outlet. Fig. 11(a) shows the simulated streamline of the cross section at line A of the JISC. The high speed jet flow impinges on the hot surface and then turns to the flow in the axial direction. As is shown in Fig. 11(b), the thickness of the boundary layer gradually increases in the radial flow region and the temperature of the fluid rises due to the absorption of heat. Owing to the confinement of the nozzle substrate, the adjacent jet flow interacts with each other and forms the vortexes. The fluid temperature in the vortex region is nearly 10 °C higher than the nozzle region, which might result in pre-heating of the inlet fluid. As is shown in Fig. 11(c), the temperature at the center of the impingement region is very low. Thanks to the extremely high stagnation heat transfer coefficient, the minimum temperature is only 44.4 °C, 4.4 °C higher than the inlet fluid temperature. However, the local heat transfer coefficient sharply drops from $2.2 \times 10^5\ W\ m^{-2}\ K^{-1}$ to only $5.1 \times 10^4\ W\ m^{-2}\ K^{-1}$, resulting in large temperature difference on the surface. The temperature difference is as large as 20 °C. Therefore, the thermal model is very important for the optimal design to decrease the temperature difference.

Above mentioned results show that the JIBC device has the best cooling performance with the aforementioned nozzle arrangement and chip structure. However, the convective heat transfer coefficient of the top surface of the JIBC is much lower than that of the HBC. Thus, if the nozzle arrangement and the chip size have changed, the HBC might have better cooling performance. Fig. 12(a) shows the total thermal resistance of the three cases changes with the nozzle diameter. With the nozzle diameter increases, the thermal resistance of the three cases increase linearly. When the nozzle diameter is larger than 500 μm, the thermal resistance of the HBC becomes lower than that of the HBC, which means that the cooling performance of the HBC is better than the JIBC when the nozzle diameter is larger than 500 μm. Because when the nozzle diameter

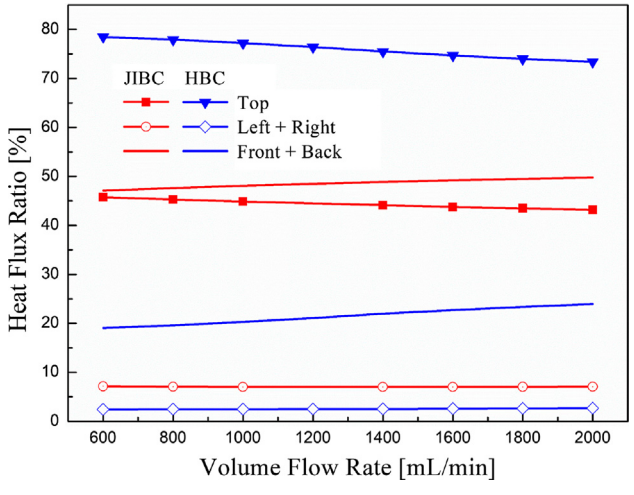

Fig. 9. Heat flux ratio of different surfaces.

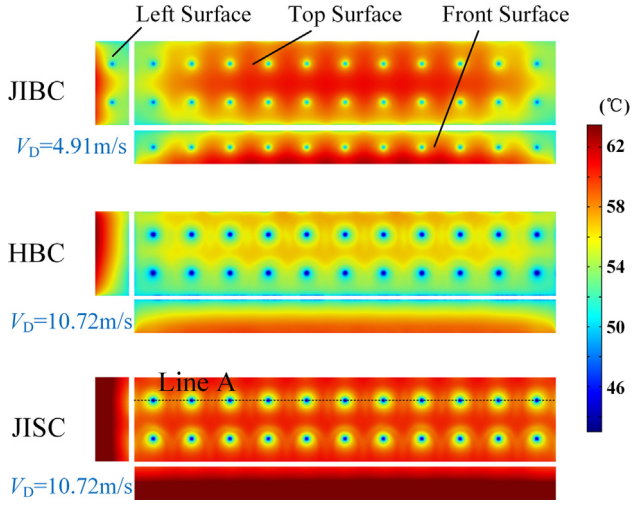

Fig. 10. The simulated temperature contour of the chip surfaces.

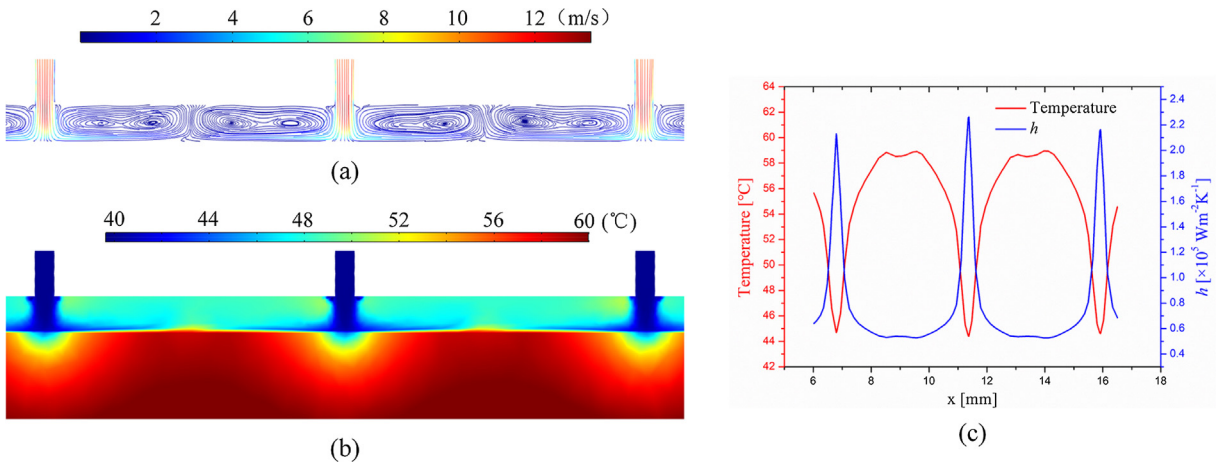

Fig. 11. (a) The streamline of the cross section at line A of the JISC, (b) the temperature distribution of the cross section at line A of the JISC and (c) the local temperature and local convective heat transfer coefficient on line A of the JISC.

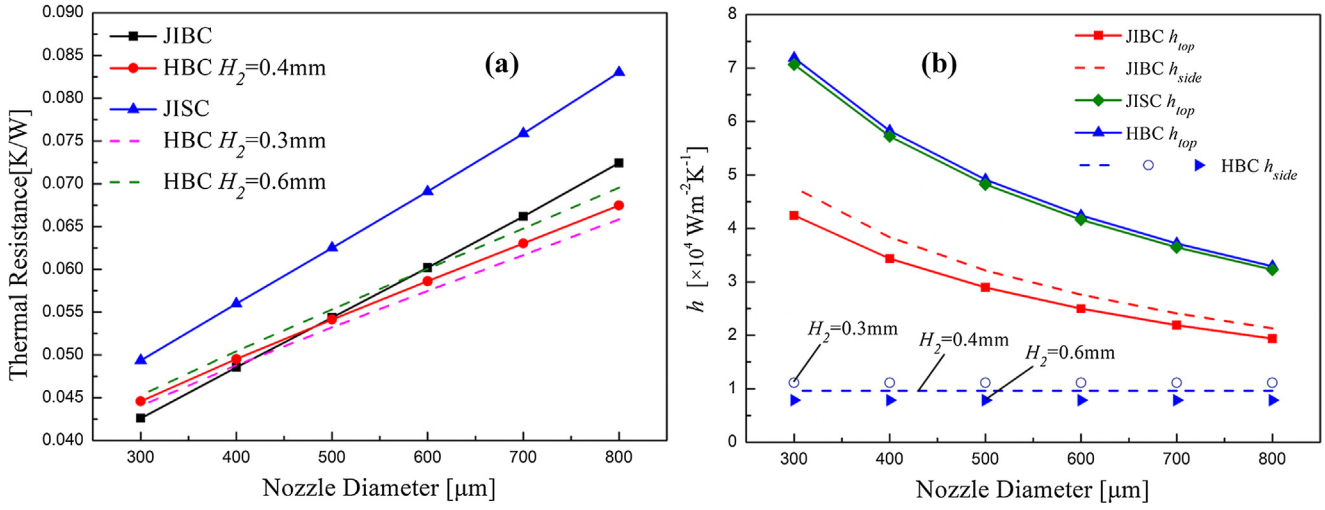

Fig. 12. (a) The total thermal resistance versus the nozzle diameter and (b) the surface *h* versus nozzle diameter.

increases, the jet impinging convective heat transfer coefficient decreases, but the channel cooling convective heat transfer coefficient does not change, as is shown in Fig. 12(b). This is owing to the fact that the flow velocity of the channel cooling is only determined by the flow rate and the cross section area of the channel, and it is independent from the nozzle arrangement. Therefore, when the H_2 increases from 0.4 mm to 0.6 mm, the cross section area of the channel increases, and the flow velocity decreases. As a result, the heat transfer coefficient h of the channel cooling decreases, leading to increasing o of the thermal resistance of the HBC. Thus, the critical nozzle diameter increases to 600 μm. On the contrary, when the H_2 is reduced to 0.3 mm, the critical nozzle diameter would decrease to 400 μm. Therefore, the cooling performance of the JIBC is not always better than the HBC when changing the nozzle arrangement, H_2 or the chip size. The developed thermal model is essential for choosing which of the three cooling method is the best under the given working condition.

6. Conclusions

In this work, we developed a jet impingement body cooling device and a channel/jet impingement hybrid body cooling device using the traditional mechanical machining method with micro-nozzles. The thermal model for the JIBC, HBC and traditional jet impingement surface cooling (JISC) was established. The thermal model is helpful to guide quick design and optimal design of the structure of the JIBC, HBD and JISC. The developed thermal model is in good agreement with the experiment. The temperature prediction error of the JIBC is less than 8.0% and that of the HBC is less than 18.1% compared with experiments. The developed JIBC device provides great cooling performance to keep the maximum chip temperature rise no more than 32 °C with the flow rate of 1500 mL/min and the heat power of 500 W. The lowest total thermal resistance of 0.041 k/W of the JIBC is achieved at the flow rate of 1800 mL/min. The heat transfer and fluid flow mechanism were investigated and analyzed by the model and simulation. It is found that when the nozzle diameter increases, the jet impinging convective heat transfer coefficient decreases, but the channel cooling convective heat transfer coefficient does not change. The flow velocity of the channel cooling is only determined by the flow rate and the cross section area of the channel, and it is independent from the nozzle arrangement. Therefore, there exist the critical nozzle diameter that determines whether the cooling performance of the JIBC is better than the HBC or not. Thus, the developed thermal model is essential for the selection and comparison of the two body cooling methods.

Conflict of interest

There are no conflicts of interest.

Acknowledgements

The authors would like to acknowledge the financial support by National Natural Science Foundation of China (51625601, 51576078, 51606074), the Ministry of Science and Technology of the Peoplés Republic of China (Project No. 2017YFE0100600), the Financial support from Creative Research Groups Funding of Hubei Province (2018CFA001).

References

[1] E. Laloya, O. Lucia, H. Sarnago, J.M. Burdio, Heat management in power converters: from state of the art to future ultrahigh efficiency systems, IEEE Trans. Power Electr. 31 (11) (2016) 7896–7908.
[2] Y. Ma, W. Lan, B. Xie, R. Hu, X. Luo, An optical-thermal model for laser-excited remote phosphor with thermal quenching, Int. J. Heat Mass Transf. 116 (2018) 694–702.
[3] B. Shang, Y. Ma, R. Hu, C. Yuan, J. Hu, X. Luo, Passive thermal management system for downhole electronics in Harsh thermal environments, Appl. Therm. Eng. 118 (2017) 593–599.
[4] S.M. SOhel Murshed, C.A. Nieto de Castro, A critical review of traditional and emerging techniques and fluids for electronics cooling, Renew. Sust. Energy Rev. 78 (2017) 821–833.
[5] X.B. Luo, R. Hu, S. Liu, K. Wang, Heat and fluid flow in high-power LED packaging and applications, Prog. Energy Combust. Sci. 56 (2016) 1–32.
[6] S. Zhou, R. Hu, X. Luo, Thermal illulsion with twinborn-like heat signatures, Int. J. Heat Mass Trans. 127 (2018) 607–613.
[7] R. Hu, S. Zhou, Y. Li, D.Y. Lei, X. Luo, C.W. Qiu, Illusion thermotics, Adv. Mater. 30 (2018) 1707237.
[8] R.C. Chu, R.E. Simons, M.J. Ellsworth, R.R. Schmidts, V. Cozzolino, Review of cooling technologies for computer products, IEEE Trans. Device Mater. Reliab. 4 (4) (2004) 568–585.
[9] A.C. Kheirabadi, D. Groulx, Cooling of server electronics: a design review of existing technology, Appl. Therm. Eng. 105 (2016) 622–638.
[10] T. Dixit, I. Ghosh, Review of micro- and mini-channel heat sinks and heat exchangers for single phase fluids, Renew. Sust. Energy Rev. 41 (2015) 1298–1311.
[11] S.T. Kadam, R. Kumar, Twenty first century cooling solution: microchannel heat sinks, Int. J. Therm. Sci. 85 (2014) 73–92.
[12] X. Hao, B. Peng, G. Xie, Y. Chen, Efficient on-chip hotspot removal combined solution of thermoelectric cooler and mini-channel heat sink, Appl. Therm. Eng. 100 (2016) 170–178.
[13] A. Sakanava, C.F. Tong, A. Nawawi, R. Simanjorang, K.J. Tseng, A.K. Gupta, Investigation on weight consideration of liquid coolant system for power electronics converter in future aircraft, Appl. Therm. Eng. 104 (2016) 603–615.
[14] B. Sun, H. Liu, Flow and heat transfer characteristics of nanofluids in a liquid-cooled CPU heat radiator, Appl. Therm. Eng. 115 (2017) 435–443.
[15] K.M.F. Shahil, A.A. Balandin, Graphene–multilayer graphene nanocomposites as highly efficient thermal interface materials, Nano Lett. 12 (2012) 861–867.
[16] C. Yuan, B. Xie, M. Huang, R. Wu, X. Luo, Thermal conductivity enhancement of platelets aligned composites with volume fraction from 10% to 20%, Int. J. Heat Mass Tran. 94 (2016) 20–28.
[17] W. Wu, H. Bostanci, L.C. Chow, S.J. Ding, Y. Hong, M. Su, J.P. Kizito, L. Gschwender, C.E. Snyder, Jet impingement and spray cooling using slurry of nanoencapsulated phase change materials, Int. J. Heat Mass Transf. 54 (2011) 2715–2723.
[18] P. Smakulski, S. Pietrowicz, A review of the capabilities of high heat flux removal by porous materials, microchannels and spray cooling techniques, Appl. Therm. Eng. 104 (2016) 636–646.
[19] G. Liang, I. Mudawar, Review of spray cooling - Part 1: Single-phase and nucleate boiling regimes, and critical heat flux, Int. J. Heat Mass Transf. 115 (2017) 1174–1205.
[20] G. Liang, I. Mudawar, Review of spray cooling – Part 2: High temperature boiling regimes and quenching applications, Int. J. Heat Mass Transf. 115 (2017) 1206–1222.
[21] G. Natarajan, R.J. Bezama, Microjet cooler with distributed returns, Heat Transf. Eng. 28 (8–9) (2007) 779–787.
[22] A. Husain, S.M. Kim, K.Y. Kim, Performance analysis and design optimization of micro-jet impingement heat sink, Heat Mass Transf. 49 (2013) 1613–1624.
[23] T. Muszynski, The influence of microjet array area ratio on heat transfer in the compact heat exchanger, Exp. Therm. Fluid Sci. 99 (2018) 336–343.
[24] C.T. Chang, G. Kojasoy, F. Landis, Confined single- and multiple-jet impingement heat transfer-I. Turbulent submerged liquid jets, Int. J. Heat Mass Transf. 38 (5) (1995) 833–842.
[25] J.A. Fitzgerald, S.V. Garimella, A study of the flow field of a confined and submerged imping jet, Int. J. Heat Mass Transf. 41 (8–9) (1998) 1025–1034.
[26] S.V. Garimella, Heat transfer and flow fields in confined jet impingement, Ann. Rev. Heat Transf. 11 (11) (2000).
[27] C.Y. Li, S.V. Garimella, Prandtl-number effects and generalized correlations for confined and submerged jet impingement, Int. J. Heat Mass Transf. 44 (2001) 3471–3480.
[28] A.J. Robinson, E. Schnitzler, An experimental investigation of free and submerged miniature liquid jet array impingement heat transfer, Exp. Therm. Fluid Sci. 32 (2007) 1–13.
[29] T.M. Bandhauer, D.R. Hobby, C. Jacobsen, D. Sherrer, Thermal performance of micro-jet impingement device with parallel flow, jet-adjacent fluid removal, Proceedings of the ASME 2018 16th International Conference on Nanochannels, Microchannels, and Minichannels, 2018.
[30] J. Jorg, S. Taraborrelli, G. Sarriegui, R.W.D. Doncker, R. Kneer, W. Rohlfs, Direct single impinging jet cooling of a MOSFET power electronic module, IEEE T. Power Electr. 33 (5) (2018) 4224–4237.
[31] M.K. Sung, I. Mudawar, Single-phase hybrid micro-channel/micro-jet impingement cooling, Int. J. Heat Mass Transf. 51 (2008) 4342–4352.
[32] Y. Han, B.L. Lau, X. Zhang, Y.C. Leong, K.F. Choo, Thermal management of hotspots with a microjet-based hybrid heat sink for GaN-on-Si deices, IEEE Trans. Compon. Packag. Manuf. Technol. 4 (9) (2014) 1441–1450.
[33] C.B. Kim, C. Leng, X.D. Wang, T.H. Wang, W.M. Yan, Effects of slot-jet length on the cooling performance of hybrid microchannel/slot-jet module, Int. J. Heat Mass Transf. 89 (2015) 838–845.
[34] A.J. Robinson, R. Kempers, J. Colenbrander, N. Bushnell, R. Chen, A single phase hybrid micro heat sink using impinging micro-jet arrays and microchannels, Appl. Therm. Eng. 136 (2018) 408–418.
[35] C. Qian, A.M. Gheitaghy, J. Fan, H. Tang, B. Sun, H. Ye, G. Zhang, Thermal management on IGBT power electronic devices and modules, IEEE Access 6 (2018) 12868–12884.
[36] M.M. Yovanovich, Thermal resistances of circular source on finite circular cylinder with side and end cooling, J. Electron. Packag. 125 (2003) 169–177.
[37] Y. Muzychka, R. Culham, M. Yovanovich, Thermal spreading resistances in rectangular flux channels: Part I Geometric equivalences, in: 36th AIAA Thermophysics Conference, 2003, p. 4187.
[38] M.-H. Carolina, D.C. Matthew, A.W. Justin, V.G. Suresh, Development and validation of a semi-empirical model for two-phase heat transfer from arrays of impinging jets, Int. J. Heat Mass Transf. 124 (2018) 782–793.
[39] H. Martin, Heat and mass transfer between impinging gas jets and solid surfaces, Adv. Heat Transf. 13 (1997) 1–60.
[40] Y. Muzychka, J. Culham, M. Yovanovich, Thermal spreading resistances of rectangular flux channels: Part II Edge cooling, in: 36th AIAA Thermophysics Conference, 2003, pp. 1–9.
[41] R. Wu, B. Duan, F. Liu, H. Wu, Y. Cheng, X. Luo, Design of a hydro-dynamically levitated centrifugal micro-pump for the active liquid cooling system, in: 18th International Conference on Electronic Packaging Technology (ICEPT), IEEE, 2017, pp. 402–406.
[42] X. Luo, F. Liu, B. Duan, H. Wu, J. Hu, X. Yu, A hydrodynamic levitated mechanical micropump, Chinese Patent, ZL 2016.1.1139270.6
[43] X. Luo, R. Wu, B. Duan, F. Liu, A hydrodynamic levitated mechanical pump with grooved bearings, Chinese Patent, ZL 201710339001.2.